



Gas-liquid mass transfer intensification for bubble generation and breakup in micronozzles

Felix Reichmann¹ · Jakob Herath¹ · Lena Mensing¹ · Norbert Kockmann¹

Received: 4 January 2021 / Accepted: 13 May 2021 / Published online: 14 June 2021
© The Author(s) 2021

Abstract

The local gas-liquid mass transfer was characterized during bubble generation in T-contactors and in an adjacent micronozzle. A colorimetric technique with the oxygen sensitive dye resazurin was investigated to visualize gas-liquid mass transfer during slug flow, bubble deformation, as well as laminar and turbulent bubble breakup in the wake of a micronozzle. Two optimized nozzle geometries from previous studies were evaluated concerning volumetric mass transfer coefficients for low pressure loss, narrow residence time distribution, or high dispersion rates. Highest values in k_1a up to 60 s^{-1} were found for turbulent bubble breakup and an optimized micronozzle design in respect to pressure drop and dispersion rate. The achieved mass transfer coefficients were correlated with the energy dissipation rate within the micronozzles and with the inverse Kolmogorov time scale in vortex dissipation in good agreement for laminar and turbulent breakup regimes.

Keywords Gas-liquid mass transfer · Micronozzle · Bubble breakup · Resazurin oxidation

Introduction

Gas-liquid reactions are highly relevant in chemistry such as for oxidation, halogenation, or hydrogenation [1–6], which play an important role for pharmaceutical and fine chemical industry [7]. In these applications, mass transfer of a gaseous component into the liquid phase is the crucial and rate-limiting step. In conventional equipment, gaseous reactants are often used in large excess due to poor interfacial mixing [8]. In case of insufficient mixing in processes including rapid reactions,

mass transport limitations can prevent the intrinsic reaction kinetics from evolving, resulting in extended reaction times, poor reactor performance, and often low product quality [9]. Here, microstructured reactors offer increased surface-to-volume ratio and benefit from large interfacial area enabling fast mixing and reduced transfer resistances [10]. Consequently, reaction rates are enhanced and gas-liquid mass transfer can be intensified applying continuous flow reactors [7]. Gas-liquid reactions in microreactors therefore have been subject to a variety of academic studies regarding hydrodynamics and mass transfer [10–18].

In gas-liquid microreactors the contacting of the two phases can be realized by either keeping both phases continuous with a stabilized interface (e.g. falling film or membrane reactor) or by dispersing one phase into the other using appropriate inlets or micromixers (e.g. T-junction, Y-contactor, flow focusing) [19]. Particularly, micromixers are employed for intense mixing as high specific interfacial area can be attained [20]. Often, the gas phase is dispersed into the liquid phase using a T-contactor and is then refined in a downstream micronozzle for increased interfacial area. The mass transfer is closely associated with two-phase flow patterns, which rely on channel characteristics, fluid properties, and process parameters. Typical flow regimes encountered in microchannel gas-liquid flow include parallel flow, slug flow, and bubbly flow

Scientific highlights:

mass transfer during bubble generation nearly constant for various flow rates
energy dissipation rate is important parameter for dispersion and mass transfer
rapid expansion after micronozzle leads to small bubble with high mass transfer
inverse Kolmogorov time scale determines the mass transfer coefficient in bubble breakup

✉ Norbert Kockmann
norbert.kockmann@tu-dortmund.de

¹ Department of Biochemical and Chemical Engineering, Laboratory of Equipment Design, TU Dortmund University, 44227 Dortmund, Germany

with respective transition regimes [21]. The interfacial area per unit volume increases from parallel flow to bubbly flow [22]; however, due to prevailing surface forces in capillaries, slug flow is encountered for the most part [23].

Converging–diverging micronozzles are used to disperse gas-liquid flow with low pressure loss, breaking up bubbles into significantly smaller ones; hence, larger interfacial area is created [24–28]. External forces, originating from the liquid, act on the phase boundary. Once the bubble preserving Laplace pressure is surpassed, bubble breakup is induced. The degree of bubble breakup is determined by energy dissipation rates [27].

In a previous fundamental study [28], various bubble breakup regimes have been characterized and breakup mechanisms have been projected. In laminar bubble breakup, binary bubble breakup or shearing off of satellite bubbles are examined at moderate flow rates. The daughter bubble size distribution has a bimodal shape and is rather broad with a significantly larger mean daughter bubble diameter than for turbulent bubble breakup. Turbulent breakup is reached at higher flow rates and mother bubbles are broken up into many small daughter bubbles of similar size. Hence, the daughter bubble size distribution is rather narrow and features a unimodal shape. Consequently, larger interfacial area is created [29]. Moreover, internal jet flow within mother bubbles were examined, which can also be used for bubble breakup [30]. Other studies were dedicated towards optimized nozzle designs regarding residence time distribution [27] and bubble breakup efficacy concerning pressure drop [28].

The range of obtained k_1a values in a straight reference channel is small and values are in the known range of Taylor and bubbly flow in microchannels as shown in Table 1. The volumetric mass transfer coefficients obtained with the nozzles are in the upper range for micro reactors [12, 35, 36].

The concluded volumetric mass transfer coefficients for bubble breakup correspond to the obtained k_1a value range found by Yang et al. [34] for bubble formation in a T-contactor, which is also a very dynamic process justifying a comparison.

In this work, mass transfer processes related to micronozzle induced bubble breakup are examined and quantified for the known bubble breakup regimes. Moreover, two optimized nozzle geometries developed by Tollkötter [27] and Reichmann et al. [28] are analyzed concerning their gas-liquid mass transfer characteristics. Measurements are based on a colorimetric method introduced by Dietrich et al. [37]. This non-invasive technique uses a colorless, reduced form of the oxygen-sensitive dye resazurin, which is oxidized to pink resorufin in the presence of oxygen, and enables the quantification of local mass transfer in the microchannel. The produced resorufin is directly proportional the oxygen uptake into the liquid phase. Finally, volumetric mass transfer coefficients k_1a are determined for the refinement of two-phase flow.

Theoretical background

Bubble generation and gas-liquid dispersion

Bubble generation is a dynamic process containing interactions of gas and liquid flow on short time and length scales [38]. In this work, primary bubble generation is carried out via a T-contactor and refinement of the two-phase flow is realized by a downstream micronozzle in order to create large interfacial area for enhanced mass transport as shown in Fig. 1.

The hydrodynamics of the continuous liquid phase are determining primary bubble generation and the refinement of two-phase flow at low void fractions [39]. In general, laminar flow and liquid Reynolds numbers $Re_l < 2300$ prevail in

Table 1 Literature values for overall volumetric mass transfer coefficient k_1a on gas-liquid mass transfer in microchannels

author	experimental characteristics	k_1a [s^{-1}]
Yue et al. [31]	<ul style="list-style-type: none"> slug flow, slug-annular, churn flow $u_g=0-2 \text{ m}\cdot\text{s}^{-1}$, $u_l=0.09-1 \text{ m}\cdot\text{s}^{-1}$ straight microchannel, $d_h=0.67 \text{ mm}$ 	0.3–21
Yang et al. [32]	<ul style="list-style-type: none"> slug flow $u_g=0.04-0.08 \text{ m}\cdot\text{s}^{-1}$, $u_l=0.16-0.27 \text{ m}\cdot\text{s}^{-1}$ straight microchannel, $d_h=0.50 \text{ mm}$ bubble formation stage (Taylor bubble) 	4.1–8.9 6.3–17.1
Zhu et al. [33]	<ul style="list-style-type: none"> bubbly flow, slug flow, annular flow $u_g=0.017-0.556 \text{ m}\cdot\text{s}^{-1}$, $u_l=0.017-0.139 \text{ m}\cdot\text{s}^{-1}$ straight microchannel, $d_h=0.40 \text{ mm}$ 	0.5–15
Yang et al. [34]	<ul style="list-style-type: none"> bubble formation stage (bubbly flow) $\mu_g=0.0035-0.0046 \text{ m}\cdot\text{s}^{-1}$, $u_l=0.01-0.03 \text{ m}\cdot\text{s}^{-1}$ T-contactor and co-flowing device 	15–77

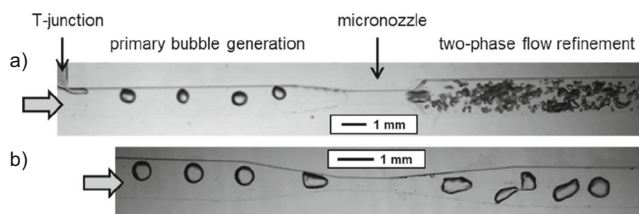


Fig. 1 Primary bubble generation in a T-contactor and refinement of gas-liquid flow in a micronozzle optimized regarding pressure drop [28] with turbulent bubble breakup (a) and in a micronozzle optimized regarding residence time distribution [27] with laminar bubble breakup (b)

straight microchannels and turbulent flow can only be achieved with comparatively high energy input [40]. In ducts, Re_l is defined by mean flow velocity u_l , the channel’s hydraulic diameter d_h , and kinematic viscosity of the liquid ν_l .

$$Re_l = \frac{u_l d_h}{\nu_l} \text{ with } d_h = \frac{2wh}{w+h} \quad (1)$$

The hydraulic diameter is described by channel width w and channel height h . Within layered flow, radial mass transfer is controlled by molecular diffusion only, which is a rather slow process in the order of seconds and minutes [41]. For $Re_l > 100$, convection contributes to the mixing process [42]. In this work, Re_l numbers in transient regime are reached by combining micro- and millichannels, keeping the pressure drop moderate at the same time. Fully turbulent flow can only be achieved with comparatively high energy input. Therefore, the mean energy dissipation rate $\bar{\epsilon}$ is an influencing parameter for mixing [7]. It is defined in Eq. (2) with total volumetric flow rate \dot{V}_{tot} , pressure loss Δp , the density ρ_l , of the liquid phase, and dissipation volume V_{diss} .

$$\bar{\epsilon} = \frac{\dot{V}_{tot} \Delta p}{\rho_l V_{diss}} \text{ with } V_{diss} = d_0 l_0 h_0 + \frac{d_0 + 3.84 d_0}{2} 16 d_0 h_1(x) \quad (2)$$

The dissipation volume relies on the geometry of the turbulence generator (hydraulic diameter d_0 , length l_0 , and height h_0 of smallest cross section) and the downstream channel depth h_1 [43]. The index “-1” relates to the converging nozzle region, index “0” to the smallest cross section, and index “1” to the diverging outlet nozzle part, see also Fig. 2. For bubble formation in T-contactors, three mechanisms of bubble formation were proposed: dripping, squeezing, and jetting. These depend on contactor geometry, flow rates, and the fluids’ properties and have an impact on mass transfer [13, 44]. Here, slug flow resulted in the T-contactor at low flow rates and bubbly flow was obtained at higher flow rates.

The breakup of these bubbles into smaller daughter bubbles in the wake of the nozzle depends on the interactions between the bubble’s surface force and the liquid’s inertia force [45, 46]. The liquid Weber number We_l puts these forces into relation [47] with surface tension σ .

$$We_l = \frac{\rho_l u_l^2 d_h}{\sigma} \quad (3)$$

The Weber number is important for the bubble generation regime.

Gas-liquid mass transfer and test reaction

Liquid side volumetric mass transfer coefficient is used for quantification of the transport of a solute from the gas phase to the liquid phase as the resistance is mainly in the liquid phase [11]. Applying film theory, the concentration change over time depends on the liquid side mass transfer coefficient k_l , the interfacial area a , the difference of equilibrium solubility concentration c^* at the interface, and the concentration in the liquid of for a given time $c(t)$.

$$\frac{dc}{dt} = k_l a (c^* - c(t)) \quad (4)$$

The mass transfer within the liquid phase is determined with the help of an oxidation reaction originating from the redox reaction network of resazurin [37]. The completely reduced form (colorless dihydroresorufin) is oxidized by pure oxygen to resorufin (pink color) and finally to resazurin with blue color. This reaction is sufficiently fast with an enhancement factor of $E = 1.03 \pm 0.01$ and a related Hatta number with $Ha_{min} = 6.66$ for microchannels [32, 48]. The chemical reaction does not significantly enhance the oxygen mass transfer into the liquid phase.

For the instantaneous reactions, the concentration of oxygen in the bulk liquid phase can be assumed as $c(t) = 0 = \text{const}$ [48]. Consequently, the driving force at the gas-liquid interface is also constant with $(c^* - 0)$, and $k_l a$ can be determined according to Eq.

$$k_l a = \frac{\Delta c}{c^* \cdot \Delta t} \quad (5)$$

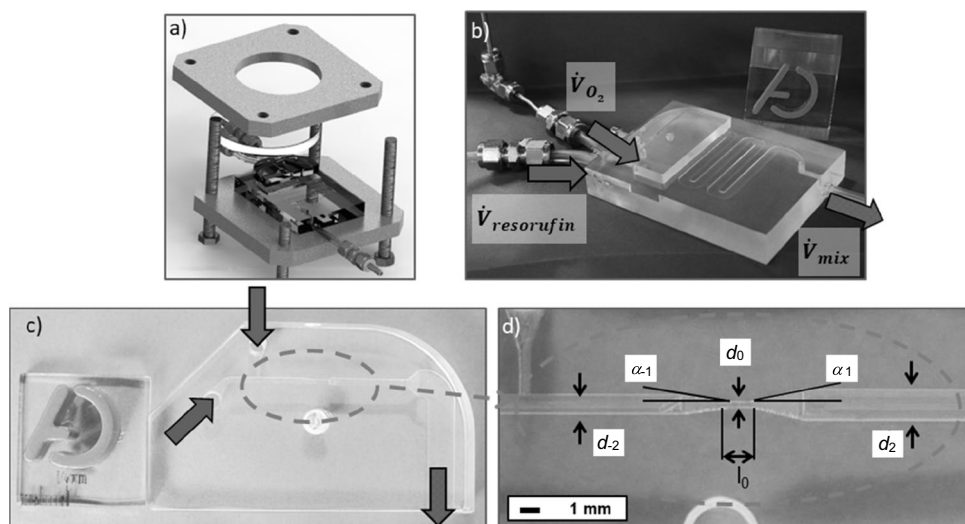
The mass transfer coefficient is proportional to the resazurin concentration at a certain location Δc divided by the oxygen saturation concentration c^* and the time of the fluid elements after the first gas-liquid phase contact. This time is the mean residence time up to the location of concentration measurement.

Experimental setup and methods

Experimental setup

The employed microreactor setup is shown in Fig. 2a and is adapted from previous works [28, 29, 49]. The microreactor consists of a reaction plate featuring a milled in flow channel

Fig. 2 a) 3D-modell of the microreactor setup in explosion view. b) Reaction plate with T-contactor and nozzle inlay. Arrows indicate inlet of gas and liquid phase and exit of the mixture. c) Close-up of the exchangeable nozzle inlay. d) Close-up of the micronozzle with geometrical parameters d_{-2} , d_0 , and d_2 for hydraulic diameter of the inlet channel, the nozzle and the outlet channel, respectively, together with the inlet and outlet angle α_{-1} and α_1 , respectively



(rectangular cross section, $w = 5 \text{ mm}$, $h = 1 \text{ mm}$) on its upper side (cf. Figure 2b). A material recess within the reaction plate allows for the quick exchange of nozzle inlays (cf. Figure 2c) and thus the simple variation of nozzle geometries. The important geometrical parameters are labeled in Fig. 2d. The microchannel is sealed with a view glass and two outer flanges, made from stainless steel, clamp the view glass and the reaction plate together. The highly transparent polymethylmethacrylate (PMMA) reaction plate and view glass, in combination with a light-emitting diode (LED) panel that is placed below the microreactor, enable optical observation of bubble breakup and mass transfer characterization using a high-speed camera from above.

Fluidic connections for liquid and gas supply and outlet flow are laterally attached to the reaction plate (cf. Figure 2b). The entire experimental setup is described in an earlier contribution [28]. The microreactor and the nozzle inlays are manufactured by high precision drilling in the mechanical workshop of TU Dortmund University. A reference element is manufactured without the micronozzle. Therefore, the pressure drop induced by adjacent channels can be determined and subtracted from the measurements using nozzle inlays to obtain solely the pressure drop caused by the micronozzle. Mass transfer within the straight reference channel is investigated and respective mass transfer coefficients serve as a benchmark for the nozzle induced mass transfer intensification. Table 2 gives an overview of different nozzle geometries.

Nozzle element N1 represents a compromise between grade of fine bubble dispersion and narrow residence time distribution within the channel developed by Tollkötter [27]. Large outlet angles induce distinct recirculation zones in the wake of the nozzle. These countercurrent flows trap bubbles so that residence time distribution is rather broad. Nozzle inlay N2 features an optimized nozzle geometry regarding bubble size and pressure drop developed by Reichmann et al. [28].

Both nozzles N1 and N2 represent optimized geometries concerning low pressure loss N1 and dispersion intensity N2 and will be investigated in the following study. The straight reference channel R serves as a reference.

Experimental parameters

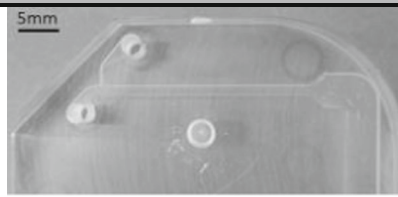

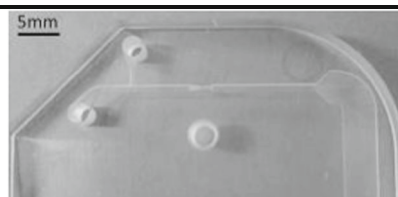
The solution for mass transfer experiments is prepared with a concentration of 0.1 g L^{-1} resazurin (Thermo Fisher Scientific Inc., USA), 0.1 M glucose (D(+)-glucose anhydrous, AnalaR NORMAPUR® for analysis, VWR Chemicals, Belgium) and 0.3 M NaOH (pellets, VWR Chemicals, Belgium). These concentrations are adopted from Dietrich et al. [37]. The colorless dihydroresorufin solution is conveyed into the microreactor at varying volumetric flow rates. However, volumetric flow rate of oxygen (Messer Group GmbH, Germany) is held constant for all presented experiments. Thus, gas content was variable despite a broad spectrum of flow and bubble breakup regimes. Total volumetric flow rates in the range of 20 mL min^{-1} and 140 mL min^{-1} are employed at resulting gas contents of $GC = 0.07\text{--}0.5$. Experiments were carried out at room temperature.

Image acquisition and processing

Images of the bubbles moving in the microchannel are recorded with a monochromatic high-speed camera (Xtra Motion NR4, Imaging Solutions GmbH, Germany). The different levels of pink coloration, which depend on the reaction progress, are represented by 256 grey values in the acquired images. The gray values correlate with the concentrations of resorufin or oxygen transferred into the solution.

The recorded images had to be digitally processed to extract an accurate quantification of the resorufin concentration, which then is converted into an equivalent oxygen concentration taking stoichiometry into account. The image processing

Table 2 Manufactured micronozzle designs for mass transfer characterization in micronozzles.

nozzle	picture	geometrical parameters
R		<ul style="list-style-type: none"> • $d = 0.75$ mm • $w = 1$ mm, $h = 0.5$ mm
N1 ²⁷		<ul style="list-style-type: none"> • $d_{-2} = 0.75$ mm, $\alpha_1 = 8^\circ$ • $w_{-2} = 1$ mm, $h_{-2} = 0.5$ mm • $d_0 = 0.5$ mm, $l_0 = 1$ mm • $w_0 = 0.5$ mm, $h_0 = 0.5$ mm • $d_2 = 0.75$ mm, $\alpha_1 = 6^\circ$
N2 ²⁸		<ul style="list-style-type: none"> • $d_{-2} = 1$ mm, $\alpha_1 = 8^\circ$ • $w_{-2} = 1$ mm, $h_{-2} = 1$ mm • $d_0 = 0.5$ mm, $l_0 = 2.5$ mm • $w_0 = 0.5$ mm, $h_0 = 0.5$ mm • $d_2 = 1$ mm, $\alpha_1 = 80^\circ$

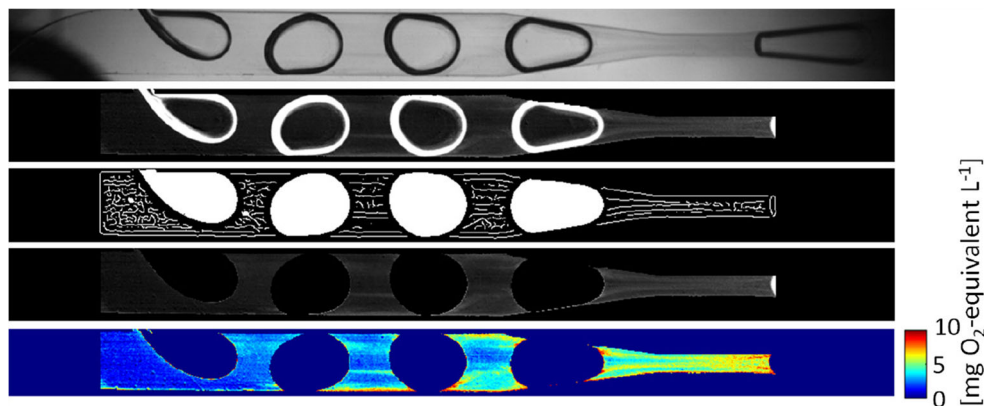
is carried out with the Image Processing Toolbox within Matlab (R2012a). The method from Dietrich et al. [37] is modified for this study and described in the following. In a first step, an averaged background image from 20 images is subtracted from the raw images to eliminate the effect irregular backlight distribution. Pictures are inverted prior to subtraction to assure increasing grey values correlate with increasing concentrations. Images are cropped to reduce necessary computing power. The interfaces of the bubbles lead to refraction and reflection of the transmitted light. The areas of the bubbles that appear dark due to light refraction and reflection are detected with the canny edge algorithm and masked in order to exclude them from analysis. Finally, a heat map is created from grey values, indicating the local concentrations along the channel. The steps are visualized in Fig. 3.

For high flow rates and turbulent bubble breakup, the canny edge algorithm reaches its limits where strongly deformed bubbles are not detected. Here, manual bubble detection and masking is carried out.

Correlation of grey values and equivalent oxygen concentration

A calibration curve was created in order to convert the grey values into equivalent oxygen concentrations. The de-facto oxygen concentration in the solution is zero due to the instantaneous reaction of the dissolved oxygen and dihydroresorufin in the liquid phase, hence, the term “equivalent” is used. The equivalent oxygen concentration can be deduced from the measured resorufin concentrations, according to Eq. (6).

Fig. 3 Image processing procedure for quantification of resorufin and equivalent oxygen concentration



Therefore, a grey value can be processed to an equivalent oxygen concentration.

$$\begin{aligned} n_{\text{O}_2, \text{transferred}} &= n_{\text{O}_2, \text{reacted}} = \frac{n_{\text{dihydroresorufin}}}{2} = \frac{n_{\text{resorufin}}}{2} \\ &= \frac{n_{\text{resazurin}}}{2} \end{aligned} \quad (6)$$

For calibration, resorufin solutions were fed into the microreactor with different concentrations and the related images were analyzed. A corresponding calibration curve, which correlates grey values and equivalent oxygen concentrations, is shown in Fig. 4 and validates the linear trend from Dietrich et al. [37]. Monochromatic pictures from resorufin solutions and respective equivalent oxygen concentration are displayed in Fig. 4b.

Results and discussion

Flow regime maps

Various liquid flow rates are investigated for dispersion at constant gas flow rate. Figure 5a shows the flow regimes in the reference channel, which are also valid for experiments using micronozzles N1 and N2 for the section upstream of the orifice with the only exception that slug/bubbly flow is observed at 35 mL min⁻¹ for N2. At high gas contents and lower total flow rates, slug flow is noticed. The Taylor bubbles always stay in contact with the channel walls and are merely stretched due to the narrower channel cross section. Bubble breakup regimes are shown in Fig. 5b and c) for nozzle inlay N1 and N2, respectively.

In case of bubbly flow in front of the nozzle, a variety of bubble behaviors were observed behind the micronozzles N1 and N2. At moderate flow rates, a deformation of bubbles was noted. Thus, external forces are not strong enough to cause a breakup. For increased total volumetric flow rates, laminar bubble breakup is noticed. Finally, turbulent bubble breakup regime is reached behind the micronozzle for total flow rates greater than 100 mL min⁻¹. For N2, slug flow adjusts in the

wake of the micronozzle at 20 and 25 mL min⁻¹. Bubble deformation occurs for 35 mL min⁻¹ and laminar breakup for 50 and 60 mL min⁻¹. Turbulent breakup regime starts at 70 mL min⁻¹ in N2.

Mass transfer measurement

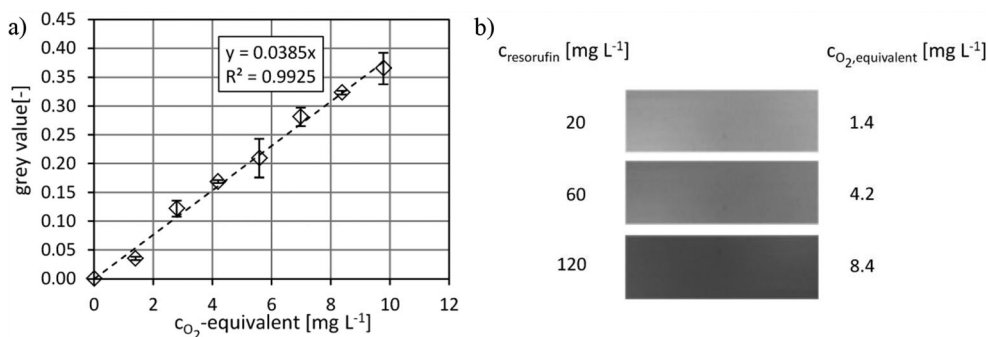
The reference channel serves as a benchmark for mass transfer using the micronozzles. Investigated flow regimes are limited to slug and bubbly flow due to their highest interfacial areas per unit volume. These regimes are also employed in mass transfer experiments using the micronozzle inlays.

Reference channel mass transfer

The flow regime and related heat maps are displayed exemplarily in Fig. 6 for the reference channel with the respective original images, the corrected images, and the heat maps featuring O₂-equivalent species concentration profiles. The slight asymmetric concentration profile originates from the 90° gas inlet channel. Since all nozzles were investigated with this generation setup there is no difference observed.

The heat map images in Fig. 6 show slug flow configuration over a total time of 9.6 ms in steps of 2.4 ms. Oxygen bubbles have been numbered for identification purposes, and flow direction is from left to right. During bubble generation in the T-contactor first O₂-equivalent species was already found between bubbles 1 and 2 at *t*₀. However, mass transfer has started, and distinct fields of higher O₂-equivalent species concentration in the upper and lower channel half, with an area of lower concentration in the channel center, have already formed between bubbles 2 and 3. Here, the formation of Taylor vortices in the liquid compartment can be seen, which is well known for slug flow in straight microchannels [49–54]. However, since *Re*_l is relatively high (*Re*_l = 153) for slug flow in microchannels, the vortices show wavy movements and the diffusion process is supported by convection. The closed Taylor vortex structure is maintained over the observed channel length, which can be seen in the liquid slugs between bubbles 4 and 5, and bubbles 5 and 6. At *t*₂, the lower part

Fig. 4 a) Calibration curve for the correlation between grey values and equivalent oxygen concentrations. b) Variation in grey values for various resorufin concentrations in the microchannel



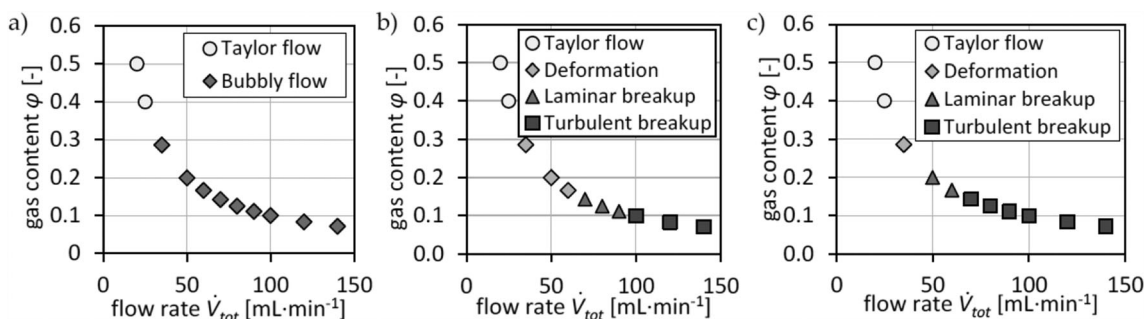


Fig. 5 a) Flow regime map for gas-liquid contacting in the T-contactor for the reference channel and upstream of nozzle inlay N1. b) Refinement regimes of gas-liquid flow downstream of the micronozzle N1. c)

Refinement regimes of gas-liquid flow downstream of the micronozzle N2. $\dot{V}_{\text{gas}} = 10 \text{ mL min}^{-1} = \text{const.}$ For all experiments

of the Taylor vortex has been completely formed between bubbles 2 and 3. The asymmetrical development of hydrodynamics and mass transfer is attributed to the eccentric bubble generation in the T-contactor. Further, a thin center line in the liquid compartment between bubbles 5 and 6 indicates high O_2 -equivalent species concentration, which is accounted for by lateral film flow between bubbles and channel walls [55]. The evolution of the thin center line can be followed, tracking the liquid slug between bubbles 3 and 4 over time (t_0 - t_4). The obtained concentration profiles correlate well with experimental results [32] and CFD simulations [56].

Micronozzle mass transfer in Taylor bubble flow

Mass transport for two-phase flow through micronozzles is qualitatively examined for the observed flow regimes up- and downstream of the nozzle in the following and exemplarily shown for micronozzle N1. The flow combination slug flow - slug flow (“flow configuration upstream of the nozzle” - “bubble behavior downstream of the nozzle”) is shown in Fig. 7 with the original and the corrected images for low total

volumetric flow rates ($\dot{V}_{\text{tot}} = 20 \text{ mL min}^{-1}$, $\text{Re}_{1,2} = 153$) and high oxygen content ($\text{GC} = 0.5$). In order to allow comparison between the flow regimes and among the reference channel and the micronozzle, a global scale 0–10 [mg O_2 -equivalent L^{-1}] is used and applied to all flow regimes.

Bubbles are formed in the T-contactor and once they enter the micronozzle, they are stretched in length before returning to their previous shape eventually behind the diverging channel. The concentration increase of O_2 -equivalent species can already be noticed in the original and the corrected image in Fig. 7. The image series is subdivided into the upstream and downstream region of the micronozzle and covers a total time span of 9.6 ms in 2.4 ms steps. Even though slug flow sets in upstream of the nozzle, a fully developed Taylor vortex cannot be observed in contrast to the straight reference channel. Here, the channel length leading to the orifice seems to be too short. Merely a slight increase in concentration can be detected in the liquid slugs between bubbles 1 and 2 and bubbles 2 and 3 (Fig. 7, t_0), respectively. However, the evolution of Taylor vortices can be sensed, since areas of higher concentrations form at the channel walls with the characteristic

Fig. 6 Image series of heat maps for mass transfer in slug flow in the reference channel R with respective local concentration profiles

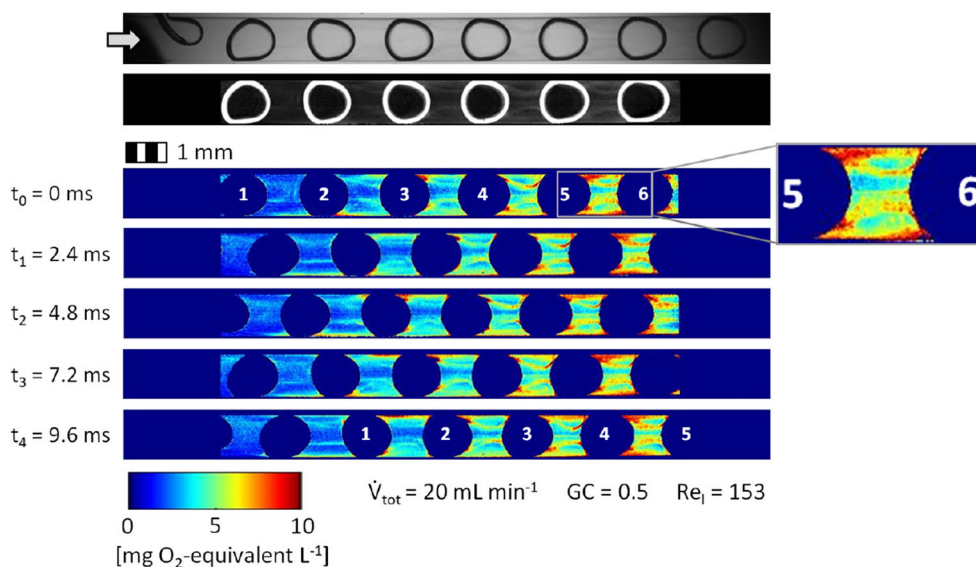
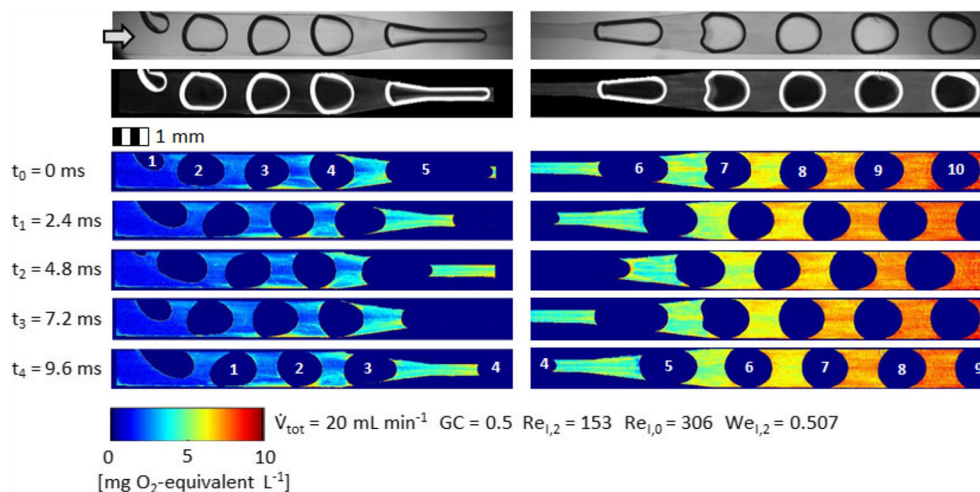


Fig. 7 Image series of heat maps for Taylor flow and bubble deformation through micronozzle N1 with respective local concentration profiles upstream (left hand side) and downstream (right hand side) of the nozzle, global scale 0–10 [mg O₂-equivalent L⁻¹]



poorly-mixed zone in the channel center between bubbles 3 and 4 (Fig. 7, t_0). The asymmetric flow development is linked to the eccentric bubble generation again.

Once a liquid slug enters the nozzle, it is stretched in length and the concentration profile seems to be homogenized across the channel width (Fig. 7, liquid slug between bubble 4 and 5 at t_2). In the diverging nozzle outlet, a well-mixed zone can be found in the channel center in the form of a thin jet, which seems to evolve from bubble 6 to bubble 7 (Fig. 7, t_0). However, this jet emerges and disappears rapidly and the concentration profile in between the bubbles homogenizes quickly and; in the end, the liquid slugs seem evenly mixed (Fig. 7, liquid slug between bubbles 9 and 10 at t_0).

Micronozzle mass transfer in laminar bubble break up

When the total volumetric flow rate is increased ($\dot{V}_{\text{tot}} = 50 \text{ mL min}^{-1}$, $\text{GC} = 0.2$, $\text{Re}_{1,2} = 613$), flow transitions to bubbly flow upstream and bubble deformation downstream of the micronozzle (Fig. 8a). Bubble train formation is observed ahead of the orifice. Downstream of the nozzle, external forces act on the bubble and actually surpass the surface tension to a multi-fold extent ($\text{We}_{1,2} = 8.12$). Nonetheless, a critical value is obviously not exceeded and the bubbles are merely deformed but not broken up, regaining their former shape eventually.

The concentration profiles upstream of the nozzle coincide with those from the bubble train formation in the reference channel. A distinct O₂-equivalent species trail can be observed between the bubbles in flow direction, representing well-mixed areas. Flow disturbances in the form of velocity fluctuation in the wake of the micronozzle seem to affect the ordered shear flow and the vortex structures in between the bubbles ($\text{Re}_{1,0} = 1226$). Hence, turbulent motions in the liquid are promoted, resulting into enhanced mass transfer from the gas into the liquid phase. Comparing bubbly flow in the straight microchannel and the one containing the nozzle,

concentrations are generally higher downstream of the orifice despite an increased flow rate and thus shorter time for mass transport.

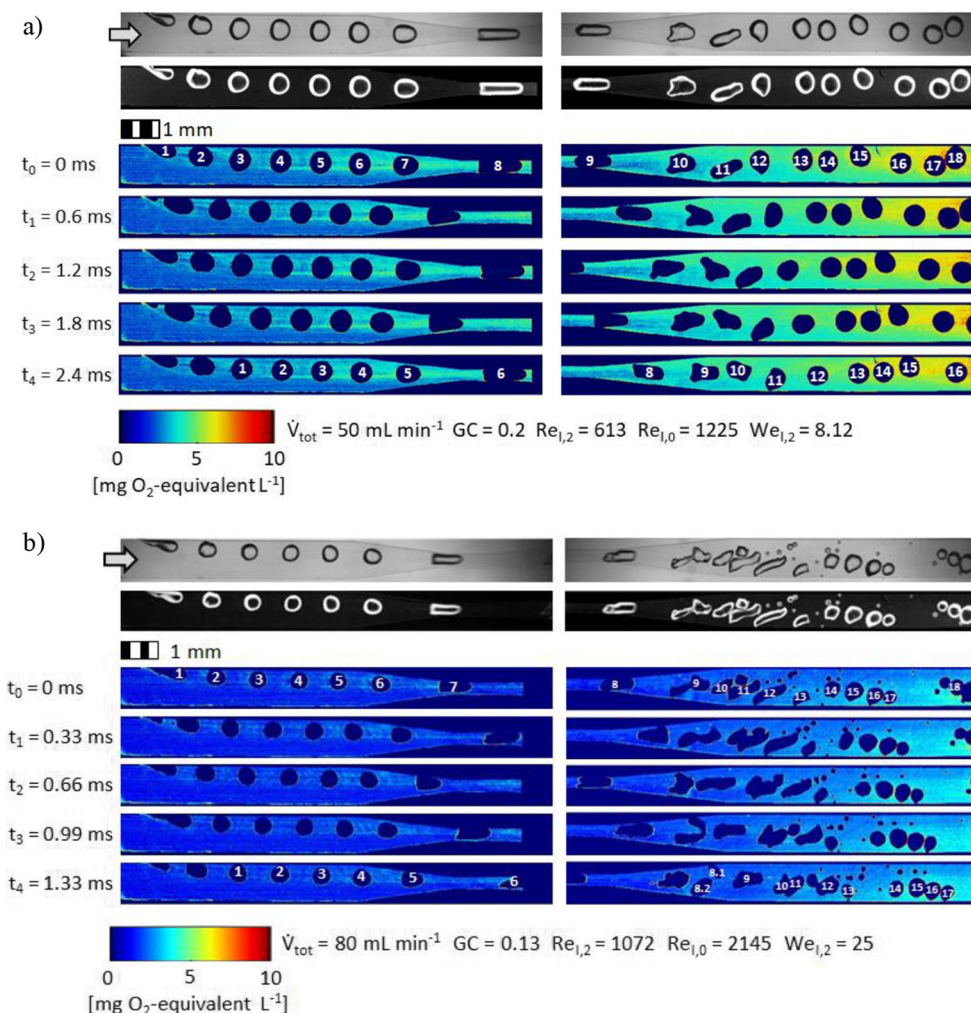
For increased flow rates of $\dot{V}_{\text{tot}} = 80 \text{ mL min}^{-1}$ and $\text{GC} = 0.13$ bubbly flow is still observed upstream of the micronozzle (Fig. 8b). However, bubbles break up in laminar regime downstream of the orifice. No significant alternations are detected in respect to bubbly flow configuration or concentration profiles upstream of the nozzle compared to the previously observed phenomena for $\dot{V}_{\text{tot}} = 60 \text{ mL min}^{-1}$. The bubbles break up in laminar regime; hence, greater mass transport area is created and an increase in mass transfer is expected. Both laminar breakup regimes are observed: binary breakup and shearing off of small satellite bubbles.

The external forces exceeded a critical value, so that the surface tension is no longer sufficiently high to keep the bubbles intact ($\text{We}_{1,2} = 25$) and; finally, the bubbles burst. Binary breakup is observed, tracking bubble 8 in the downstream images over time in Fig. 8 b). At t_0 , bubble 8 is stretched in length due to the smaller cross section and accelerated core flow. The bubble is then decelerated, compressed (t_1 and t_2), and takes a characteristic dumbbell shape at t_3 . Once a critical neck diameter is exceeded [27], the bubble splits into two daughter bubbles (t_4). The little, unnumbered bubbles over the course of the channel result from shearing off mechanism. A clear increase in concentration is found across the complete channel further downstream. Nonetheless, a slight gradient is present across the channel width with higher concentrations at the lower channel wall, which can be explained by the flow around the bubbles and the bubbles' path through the channel. A rise in concentration is found at the location of bubble breakage hinting to an intensification of mass transfer.

Micronozzle mass transfer in turbulent bubble break up

Turbulent bubble breakup is observed in the micronozzle N1 for a flow rate of $\dot{V}_{\text{tot}} = 120 \text{ mL min}^{-1}$ ($\text{Re}_{1,0} = 3370$, $\text{Re}_{1,2} =$

Fig. 8 Picture series of heat maps for bubbly flow through the micronozzle N1 and laminar bubble breakup at $Re_{1,2} = 613$ (a) and 1071 (b) with respective local concentration profiles at global scale 0–10 [mg O₂-equivalent L⁻¹]. The flow regime in b) can also be treated as transition to turbulent regime, since smaller daughter bubble appear



1685) and an oxygen content of $GC = 0.08$. Corresponding heat map images are shown in Fig. 9 for O₂-equivalent species concentration. Upstream of the nozzle, bubbly flow is observed; however, bubble diameter is smaller compared to previous flow rates and gas contents. Nonetheless, two O₂-equivalent species trails are still detected between the bubbles,

hence, the focus is only on the region of bubble breakup. Bubble movement and deformation indicate strong dynamics in the wake of the smallest cross section and the external forces tear the mother bubbles apart ($We_{1,2} = 61$). Numerous, significantly smaller daughter bubbles are generated and an increased phase boundary is obtained.

Fig. 9 Picture series of heat maps for bubbly flow through the micronozzle N1 and turbulent bubble breakup behind it with respective local concentration profiles at global scale 0–10 [mg O₂-equivalent L⁻¹]

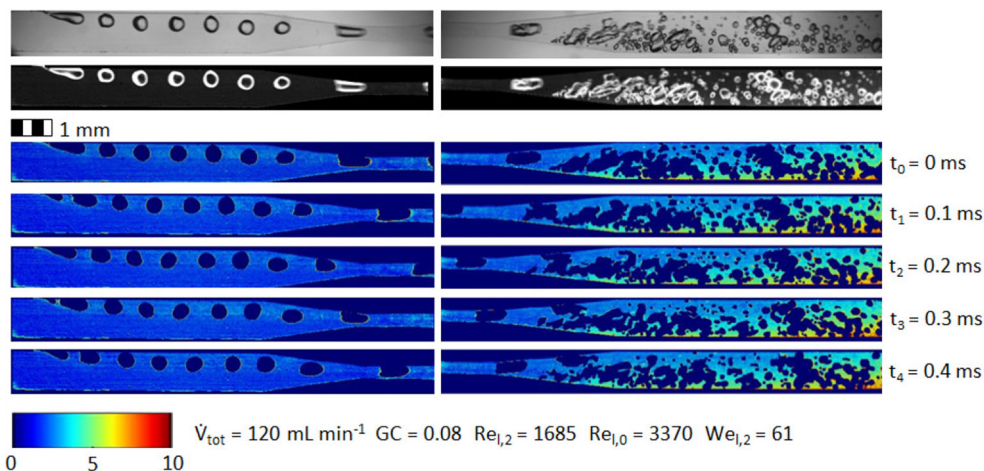


Figure 9 depicts heat map images of O₂-equivalent species concentration for bubbly flow through the micronozzle at global scale for a time span of 0.4 ms in 0.1 ms steps. No significant increase in concentration can be seen ahead of the smallest cross section and in the smallest cross section. However, shortly ahead of the end of the divergent nozzle outlet there is a distinct rise in concentration, particularly, next to the lower channel wall. This location marks the starting point of bubble breakup, too. The increase in concentration occurs mainly at the lower channel wall, but with some distance to the nozzle. Higher concentrations are found across the entire channel width. Despite a significantly shorter residence time in the observed area due to higher flow rates, the obtained concentrations are actually slightly higher in Fig. 9 than for laminar breakup in Fig. 8 b) indicating an intensified mass transfer).

Quantitative mass transfer evaluation

Reference channel - concentration profiles

In order to evaluate the mass transfer in the investigated channels, O₂-equivalent species concentrations for various flow rates are determined along the channel length and displayed in Fig. 10 over the respective time. The concentration is drawn over the mean flow time connected with the respective position in the channel. Total superficial velocities are used for this purpose, which are in very good agreement with velocities determined by bubble tracking over a defined amount of time and channel length in image analysis.

In general, the equivalent O₂-equivalent species concentrations increase over the observed channel section for slug and bubbly flow within the straight reference microchannel, which corresponds well with studies by Krieger et al. [51] and Yang et al. [32]. The filled symbols originate from linear regressions fitting the respective experimental data in positions from -2 to 2, which have been introduced for the micronozzles. All coefficients of determination are $R^2 > 0.97$ for the linear trends and indicate a good linear fit. Light grey filled symbols resemble slug flow and black ones portray bubbly flow configuration in the reference channel. Higher flow rates show decreasing slopes of the graphs. Therefore, largest concentration increase is found for slug flow at $\dot{V}_{\text{tot}} = 20$ and 25 mL min^{-1} with $Re_{1,2} = 153$ and 230 . The regime transitions to bubbly flow for higher flow rates ($\dot{V}_{\text{tot}} = 35\text{--}140 \text{ mL min}^{-1}$) and a smaller increase in concentration is found with the smallest gain for 140 mL min^{-1} . Reynolds numbers are in the range of $383 < Re_{1,2} < 1991$ indicating mainly laminar flow.

A distinct drop to lower concentrations at position -2, which is right behind the T-contactor, is evident between 50 and 60 mL min^{-1} and can be explained by the transition in bubble formation mechanism from dripping to jetting.

The time a bubble remains in the considered area must be considered, when this data is evaluated regarding mass transfer coefficients. The residence time within the considered area decreases with increasing volume flows. In Fig. 10b, concentrations are plotted over the mean flow time until positions from -2 to 2 are reached. As the mean velocity in the reference channel remains constant for a specific flow rate, the linear interrelationship between concentration and channel length transfers to

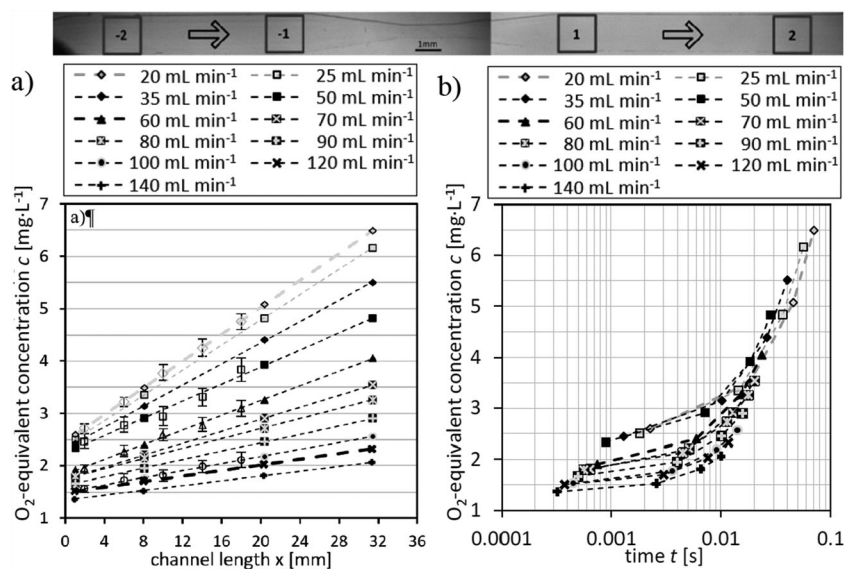


Fig. 10 a) Concentrations are plotted over the course of the reference channel for various flow rates. Unfilled symbols resemble concentrations obtained from experiments. Standard deviations for every measured concentration are exemplarily shown for four experiments. Linear trend lines are added and used to extrapolate concentrations between the positions -2 and 2. The channel positions in the diagram a) can be roughly transferred to the top image by the length

scale. Light grey filled symbols resemble Taylor flow and black symbols display bubbly flow regime. Highlighted, thicker lines are representative for the observed regimes. b) Concentrations between positions -2 and 2 for the investigated volumetric flow rates plotted over time until the respective position is reached by the flow. For higher clarity the time scale is plotted on a logarithmic scale

concentration and flow time. From the slope m of the graphs and taking c^* ($c^* = 8 \text{ g L}^{-1}$) into account, volumetric mass transfer coefficient k_1a can be obtained using Eq. (5). A logarithmic scaling of the time axis is selected here for a clearer data presentation; however, the linear rise of concentration over time is obscured and compressed due to the logarithmic display. The graphs' slopes are very similar, indicating a narrow span of mass transfer coefficient values for flow in the reference channel.

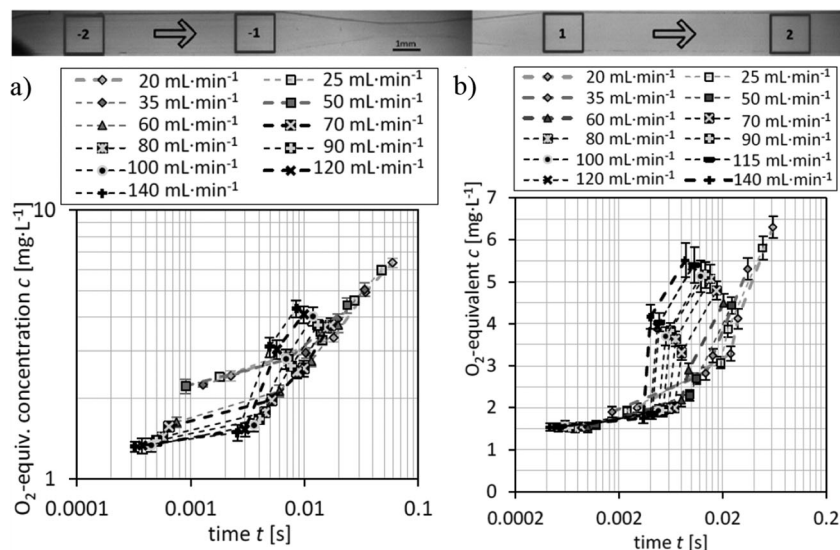
Micronozzle N1 and N2 - concentration profiles

The O_2 -equivalent species concentrations from experiments using micronozzle N1 and N2 are displayed in Fig. 11. Highlighted data (thicker lines) are characteristic for the respective flow regimes. The concentration increase across the observed area is the largest for slug flow ($\dot{V}_{\text{tot}} = 20, 25 \text{ mL min}^{-1}$, light grey filled symbols). In this regime, the graphs' courses are similar to the ones from the reference channel as the concentration increase takes an approximate linear progression over the channel length. For micronozzle N1 in Fig. 11a, the gradient between position -1 and 1 is reduced slightly employing the nozzle. Due to the narrower channel cross section and accelerated flow, the nozzle section is passed in shorter time. Hence, there is less time for the mass transfer to progress as the superordinate flow regime is maintained across the smallest cross section, and mass transport is not significantly enhanced, which explains the bend in the graphs. Reynolds numbers within the smallest cross section take values of $\text{Re}_{1,0} = 306$ and 460 , respectively. Downstream of the nozzle the flow is gradually decelerated, and Reynolds numbers are $\text{Re}_{1,2} = 153$ and 230 . Consequently, the influence of the nozzle in terms of mass transfer enhancement seems to be rather small in slug flow regime. Weber numbers are $\text{We}_{1,2} = 0.507$ and $\text{We}_{1,2} = 1.141$; yet, bubbles do not break up despite inertia force exceeding surface tension for $\dot{V}_{\text{tot}} = 25 \text{ mL min}^{-1}$.

At higher flow rates, bubbly flow sets in upstream and bubble deformation downstream of the nozzle ($\dot{V}_{\text{tot}} = 35, 50, 60 \text{ mL min}^{-1}$, dark grey filled symbols). Compared to slug flow, the overall mean gradient declines, which is also observed in the straight reference channel for increasing flow rates. The bend in the graphs' courses across the nozzle section gets more and more pronounced. Here, mass transport intensification is not strong enough to compensate for the shorter time spent in the nozzle section. Reynolds numbers behind the nozzle take values of $\text{Re}_{1,2} = 383, 613, \text{ and } 766$, respectively. Even higher values are reached within the smallest cross section with $\text{Re}_{1,0} = 766, 1225, \text{ and } 1531$ while laminar flow is the superordinate flow type. Weber numbers take values of $\text{We}_{1,2} = 3.17, 8.12, \text{ and } 12.68$. However, external forces are not sufficiently high in order to break the bubbles.

Once the bubbles begin to break up behind the micronozzle in laminar regime ($\dot{V}_{\text{tot}} = 70, 80, \text{ and } 90 \text{ mL min}^{-1}$, black symbols containing crosses), a turning point is reached. The gradient between positions -2 and -1 continues to decline with increased volume flow. However, the steady drop in concentration in position 1 with increasing flow rates comes to an end; hence, the concentration in position 1 for 90 mL min^{-1} is above the one for 80 mL min^{-1} despite a shorter residence time in the channel up to that location. Mass transport processes seem to be strongly enhanced, significantly outweighing shorter residence times. Furthermore, it is characteristic for this regime that the slope of the graph behind the nozzle is steeper than the slope of the graph ahead of the nozzle. This is probably due to the larger mass transfer area resulting from bubble breakup and the multi-directional motions intensifying the flow around the bubbles and consequently the gas-liquid mass transfer. Reynolds numbers equal $\text{Re}_{1,2} = 919, 1072, \text{ and } 1225$ behind the nozzle and $\text{Re}_{1,0} = 1838, 2144, \text{ and } 2450$ within the smallest cross section. The increased inertial forces of the fluid acting on the bubbles and finally lead to their

Fig. 11 Concentrations in positions from -2 to 2 are plotted over time until the respective position is reached by the flow for nozzle N1 in **a**) and for N2 in **b**)



binary breakup or shearing off of satellite bubbles with $We_{1,2} = 18.26, 24.85,$ and 32.46 for the respective flow rates.

For turbulent bubble breakup regime ($\dot{V}_{tot} = 100, 120,$ and 140 mL min^{-1} , black symbols), the concentration increases in position 1 continues as recirculation zones evolve in the wake of the nozzle. The concentration gradients across the nozzle section are clearly steeper than the mean gradients across the complete channel length for this regime. The slopes downstream of the nozzle are significantly increased compared to the one ahead of the nozzle, presumably due to the increased interfacial area and the turbulent motions, which lead to intensified flow around the bubbles. Reynolds number rise to $Re_{1,2} = 1379, 1685,$ and 1991 behind the micronozzle and $Re_{1,0} = 2758, 3370,$ and 3982 in the smallest cross section indicating transition to turbulent flows. Weber numbers take values of $We_{1,2} = 41.09, 61.38,$ and 85.72 .

The data from experiments using micronozzle N2 is presented in Fig. 11b. Highlighted data (thicker lines) are characteristic for the respective flow regime. The concentration along the microchannel length are following in general the observed trends from nozzle N1. An approximate linear increase in concentration over channel length is noticed for slug flow ($\dot{V}_{tot} = 20, 25 \text{ mL min}^{-1}$) while the trend for bubbly flow in the upstream region and laminar bubble breakup behind the nozzle ($\dot{V}_{tot} = 50$ and 60 mL min^{-1} , dark grey filled symbols) shows a reverse trend with increasing concentrations in position 1. The flow is decelerated more abrupt due to a larger outlet angle for N2 and velocity fluctuations occur at lower flow rates compared to N1. The predominant laminar breakup mechanism in nozzle N2 is bubble shearing at $We_{1,2} = 6.09$ and 9.51 , respectively.

The gradients across the nozzle section grow steeper for turbulent bubble breakup ($\dot{V}_{tot} = 70, 80, 90, 100, 115, 120,$ and 140 mL min^{-1} , black squared symbols containing crosses and black symbols). Within a few milliseconds the concentrations in position 1 jump to higher levels. The Weber numbers behind the micronozzle range from $13.7 < We_{1,2} < 64.3$.

Mean flow times have to be considered once again regarding mass transfer evaluation and; consequently, Fig. 11b shows concentrations applied over time for the employed flow rates. In general, the same applies to N2 as to N1; the higher the flow velocity, the shorter the average residence time in the area under consideration. In addition, the concentrations in positions -2 and -1 decrease continuously the higher the flow rate is and the slopes of the graphs within the micronozzle section grow steeper and steeper. The jump to higher concentrations between positions -1 and 1 in bubble breakup regimes is even more precipitous for N2 than for N1. The trend reversal in terms of rising concentrations in positions 1 and 2 for higher flow rates is already detectable at 50 mL min^{-1} in Fig. 11b.

Mass transfer coefficients for R, N1, and N2

The concentration and time difference between positions -2 and 2 are the important parameters in terms of volumetric

mass transfer coefficient and they are plotted over flow rate in Fig. 12a. The time difference steadily declines with increasing flow rates for the reference channel, nozzle N1, and nozzle N2. Time is reciprocally proportional to volume flow rate explaining the hyperbolic course of the graphs. The mean flow time from -2 and 2 is slightly lower for the nozzles due to the narrower cross section and resulting flow acceleration. The dissimilarity between the nozzle inlays is marginal.

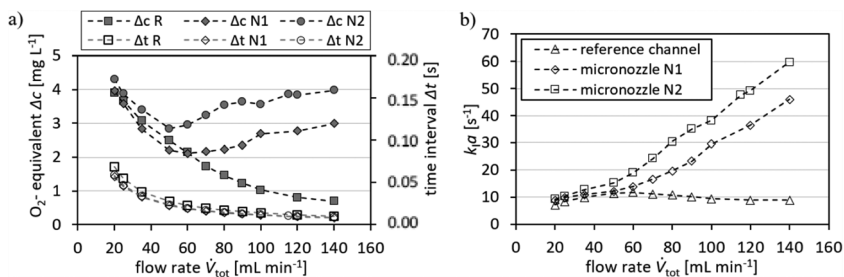
The concentration difference between positions -2 and 2 steadily declines for the reference channel R, too. The flow is not disturbed along the channel length, where laminar flow regimes prevail as residence time decreases simultaneously, resulting in less time for mass transfer. All three concentration graphs take a similar progression up to 50 mL min^{-1} . For N2, a minimum in concentration difference is reached here and the concentration difference increases again when reaching bubble breakup regimes. The transition to bubble breakup occurs at 70 mL min^{-1} for N1 with a minimum at 60 mL min^{-1} . Bubble breakup leads to an increase in concentrations despite shorter residence times in the observed region.

Finally, volumetric mass transfer coefficients between positions -2 and 2 are determined with Δt , Δc , and the saturation concentration $c^* = 8 \text{ g L}^{-1}$ according to Eq. (5). The results for all inlays are displayed in Fig. 12b. In the reference channel R, k_1a values increase with higher flow rates initially. The flow regime in the reference channel transitions from slug to bubbly flow between 25 and 35 mL min^{-1} , where bubbly flow features larger interfacial area per unit volume leading to the initial rise. Then, the slope declines, and a maximum is reached at 60 mL min^{-1} . Subsequently, the k_1a values decrease in asymptotic behavior with larger volume flows.

For nozzle N1, the graph's course is similar to the one of the reference channel R up to 50 mL min^{-1} . Bubble deformation is observed in N1 at $35, 50,$ and 60 mL min^{-1} and laminar bubble breakup is observed for $70, 80,$ and 90 mL min^{-1} . Apparently, the influence of the nozzle is already existent for $\dot{V}_{tot} \leq 50 \text{ mL min}^{-1}$ as k_1a values are slightly higher than the ones in the reference channel for a given flow rate. Pressure drop for 50 mL min^{-1} is 19 mbar and, therefore, only slightly higher than for the reference channel. Thus, the impact of the nozzle on mass transfer rises significantly for $\dot{V}_{tot} \geq 60 \text{ mL min}^{-1}$ and bubble breakup. Particularly, once bubble breakup is reached, the two graphs diverge greatly with considerably higher mass transfer coefficients for nozzle N1. A maximum pressure drop of 150 mbar is measured at 140 mL min^{-1} with a $k_1a = 46 \text{ s}^{-1}$.

In micronozzle N2, even higher mass transfer coefficients are reached; however, they come at the cost of higher pressure drop. The graph's course is similar to the one of N1 for $\dot{V}_{tot} \leq 50 \text{ mL min}^{-1}$. For higher flow rates and bubble breakup, the two graphs diverge and nozzle N2 provides highest k_1a values. Pressure drop is in the range of $16\text{--}520 \text{ mbar}$. Highest k_1a value is obtained for 140 mL min^{-1} with $k_1a = 60 \text{ s}^{-1}$. The

Fig. 12 **a)** Concentration and time differences between positions -2 and 2 over flow rate for the reference channel R, micronozzle N1, and micronozzle N2. **b)** Mass transfer coefficients for the region between positions -2 and 2 over flow rate for the reference channel R, micronozzle N1, and micronozzle N2



volumetric mass transfer coefficients obtained with the nozzle are in the upper range of microreactors.

Pressure drop and mass transfer rate

In order to evaluate a cost/benefit ratio, the pressure drops are presented and the mean energy dissipation rates are linked to the overall mass transfer coefficients. As the reference channel pressure drop is subtracted to exclude pressure drops from the inlets or the downstream meandering channel, only the pressure loss induced by the micronozzle is accessed (between positions -1 and 1). However, pressure drop and mass transfer have to be evaluated for the identical channel region and volumetric mass transfer coefficients between positions -2 and 2 have been assessed before. Therefore, the theoretical pressure drop of the straight channel sections -2 to -1 and 1 to 2 is calculated and added to the experimentally determined value from the micronozzle, represented by the unfilled symbols. Nevertheless, the graphs do not differ much to those excluding the adjacent channel sections. In general, higher pressure drop is induced by N2 compared to N1, which is most probably based on flow detachment and more intensive recirculation zones in the wake of the nozzle [57].

The pressure loss coefficients obtained in the experiments over mean Reynolds number for nozzle inlays N1 and N2 decrease with increasing Reynolds number; however, they take constant values for $Re_m \geq 1500$. Larger pressure loss coefficients are obtained for nozzle N2, which is based on the increased pressure drop despite similar flow velocities.

Figure 13 shows $k_1 a$ values (channel region -2 - 2) plotted over experimental mean energy dissipation rates obtained for the micronozzle region (pos. -1 - 1) and for calculated mean energy dissipation rates resembling the sum of experimental values for the micronozzle region and theoretical values for the adjacent channels (pos. -2 to 2). The data are separately fit with power law trend lines (dashed lines in grey) for bubble breakup and no bubble breakup. Coefficients of determination are $R^2 \geq 0.93$ indicating good fits. Deviations of -15% and +15% are indicated with dotted lines in black. Hence, an increasing mass transfer coefficient comes at the cost of higher energy input into the system. However, these correlations are not dimensionally accurate. Thus, in the next step, mean energy dissipation rate is related to the kinematic viscosity ν_1 and the square root of the quotient is taken, matching the unit from $k_1 a$ with s⁻¹. This quotient is the inverse Kolmogorov time scale in vortex dissipation [33].

The fitting with linear trend lines of data in Fig. 13 reveals high accuracy and allows for predicting mass transfer coefficients based on energy input and kinematic viscosity. A trendline is assigned to each of the flow regimes: no bubble breakup, laminar bubble breakup, and turbulent bubble breakup. An overview of the corresponding equations is presented in Table 3. A fit encompassing laminar and turbulent breakup is additionally given, also displaying high accuracy.

For low flow rates and energy input, the $k_1 a$ values remain at a constant level. Once bubble breakup begins at approximately $(\bar{\epsilon} / \nu_1)^{0.5} \approx 28.800 \text{ s}^{-1}$ (for both nozzle inlays), $k_1 a$ increases. The corresponding trend lines for the individual

Fig. 13 Overall mass transfer coefficient determined between positions -2 and 2 plotted over mean energy dissipation rate

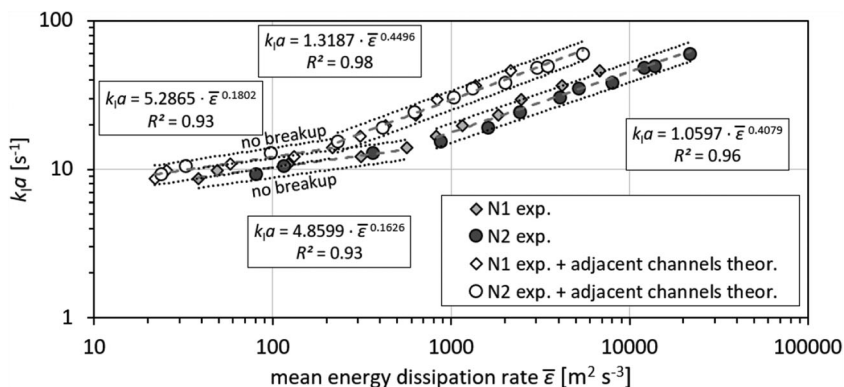


Table 3 Overview of trend lines from Fig. 13. Also, trend line equations encompassing laminar and turbulent regime are shown, where the bold data are valid over the entire investigated range

Data	regime	trend line from $k_1a=A(\bar{\epsilon}/\nu_l)^{0.5}+B$		coefficient of determination
N1 & N2 exp.	no breakup	A: 2.794·10 ⁻⁴	B: 7.3164 [s ⁻¹]	R ² =0.95
	laminar breakup	4.092·10 ⁻⁴	4.3088	R ² =0.86
	turbulent breakup	3.012·10 ⁻⁴	14.604	R ² =0.96
	breakup (lam. & turb.)	3.682·10⁻⁴	7.5264	R² = 0.94
N1 & N2 exp. + adj. Channels calc.	no breakup	A: 4.699·10 ⁻⁴	B: 7.2086 [s ⁻¹]	R ² =0.91
	laminar breakup	8.948·10 ⁻⁴	1.1339	R ² =0.98
	turbulent breakup	6.679·10 ⁻⁴	10.595	R ² =0.96
	breakup (lam. & turb.)	7.782·10⁻⁴	4.7290	R² = 0.97

regimes are presented for no bubble breakup and bubble breakup.

Conclusion

Since gas-liquid mass transfer is often limiting chemical reactions in flow reactors, a colorimetric method based on the oxygen sensitive dye resazurin is used in order to visualize and quantify mass transfer during the refinement of two-phase flow using micronozzles. Mass transfer phenomena are shown for slug flow through micronozzles, bubble deformation, laminar bubble breakup, and turbulent bubble breakup. The gas-liquid mass transfer is quantified for these regimes concerning volumetric mass transfer coefficient k_1a and benchmarked against mass transport in a straight reference microchannel. Moreover, two nozzle designs are evaluated. The reference channel yields mass transfer coefficients in the range of 7–12 s⁻¹ for slug and bubbly flow with higher values for the latter as more interfacial area per unit volume is evident. A nozzle design optimized in respect to pressure loss and residence time distribution of the gaseous phase and bubble diameter yields mass transfer coefficients in the range of 9–46 s⁻¹. Mass transfer is greatly enhanced for bubble breakup in the wake of the nozzle and highest values are reached for turbulent breakup at the costs of slightly elevated pressure drop. The optimized nozzle design, in respect to pressure drop and bubble diameter, yields even higher k_1a values in the range of 9–60 s⁻¹. For slug flow and bubble deformation the micronozzles produce similar results; yet, diverge for higher flow rates with improved results for the optimized pressure drop design. The achieved mass transfer coefficients are correlated with the energy dissipation rate within the micronozzles. A correlation is derived based on the inverse Kolmogorov time scale in vortex dissipation with good agreement. Micronozzles in combination with millichannels present a great opportunity to enhance gas-liquid mass transfer.

Abbreviations GC, gas content; LED, light emitting diode; N1, nozzle design 1; N2, nozzle design 2; O₂, oxygen; pos, position; PMMA, polymethylmethacrylate; R, reference channel

Subscripts and superscripts *, solubility concentration.; -2, position -2, upstream channel.; -1, position -1, nozzle inlet.; 0, position 0, smallest cross section.; 1, position 1, nozzle outlet.; 2, position 2, downstream channel.; diss, dissipation.; l, liquid.; tot, total.

Latin letters A, coefficient, -.; B, coefficient, s⁻¹.; c, concentration, kg L⁻¹.; d_h , hydraulic diameter, m.; E, enhancement factor, -.; h, channel height, m.; Ha, Hatta number, -.; k_1a , volumetric mass transfer coefficient, s⁻¹.; l, length, m.; n, amount of substance, mol.; p, pressure, Pa.; Re, Reynolds number, -.; Re_{1,0}, Reynolds number in the nozzle, -.; Re_{1,2}, Reynolds number in the outlet channel, -.; Re_l, Reynolds number of the liquid phase, -.; t, time, s.; u, mean flow velocity, m s⁻¹.; \dot{V} , volumetric flow rate, L s⁻¹.; V, volume, m³.; w, channel width, m.; We, Weber number, -.; We_{1,0}, Weber number in the nozzle, -.; We_{1,2}, Weber number in the outlet channel, -.; We_l, Weber number of the liquid phase, -.; x, channel length, mm.

Greek letter A, angle, °.; Δ, difference.; $\bar{\epsilon}$, mean energy dissipation rate, m² s⁻³.; ν, kinematic viscosity, m² s⁻¹.; ρ, density, kg m⁻³.; σ, surface tension, N m⁻¹.

Acknowledgments The authors would like to thank the Mechanical Workshop of TU Dortmund University for excellent manufacturing of the micronozzle equipment. Additionally, we would like to acknowledge C. Schrömgies (Laboratory of Equipment Design) for technical assistance.

Availability of data and material Not applicable.

Code availability Not applicable.

Funding Open Access funding enabled and organized by Projekt DEAL.

Declarations

Conflicts of interest/competing interests The authors declare that they have no known conflicts of interest/competing interests.

Open Access This article is licensed under a Creative Commons Attribution 4.0 International License, which permits use, sharing, adaptation, distribution and reproduction in any medium or format, as long as you give appropriate credit to the original author(s) and the source, provide a link to the Creative Commons licence, and indicate if changes were made. The images or other third party material in this article are included

in the article's Creative Commons licence, unless indicated otherwise in a credit line to the material. If material is not included in the article's Creative Commons licence and your intended use is not permitted by statutory regulation or exceeds the permitted use, you will need to obtain permission directly from the copyright holder. To view a copy of this licence, visit <http://creativecommons.org/licenses/by/4.0/>.

References

1. Yasukawa T, Ninomiya W, Ooyachi K, Aoki N, Mae K (2011) Efficient oxidative dehydrogenation of lactate to pyruvate using a gas–liquid micro flow system. *Ind Eng Chem Res* 50(7):3858–3863
2. Leclerc A, Alamé M, Schweich D, Pouteau P, Delattre C, de Bellefon C (2008) Gas-liquid selective oxidations with oxygen under explosive conditions in a micro-structured reactor. *Lab Chip* 8(5):814–817
3. Khinast JG, Koynov AA, Leib TM (2003) Reactive mass transfer at gas–liquid interfaces: impact of micro-scale fluid dynamics on yield and selectivity of liquid-phase cyclohexane oxidation. *Chem Eng Sci* 58(17):3961–3971
4. Rehm TH, Berguerand C, Ek S, Zapf R, Löb P, Nikoshvili L, Kiwi-Minsker L (2016) Continuously operated falling film microreactor for selective hydrogenation of carbon–carbon triple bonds. *Chem Eng J* 293:345–354
5. Wada Y, Schmidt MA, Jensen KF (2006) Flow distribution and Ozonolysis in gas–liquid multichannel microreactors. *Ind Eng Chem Res* 45(24):8036–8042
6. Cantillo D (2017) Halogenation of organic compounds using continuous flow and microreactor technology. 2(1):7–19
7. Kockmann N, Roberge DM (2009) Harsh reaction conditions in continuous-flow microreactors for pharmaceutical production. *Chem Eng Technol* 32(11):1682–1694
8. Mallia CJ, Baxendale IR (2015) The use of gases in flow synthesis. *Org Process Res Dev* 20(2):327–360
9. Kashid MN, Kiwi-Minsker L (2009) Microstructured reactors for multiphase reactions: state of the art. *Ind Eng Chem Res* 48(14):6465–6485
10. Kashid MN, Renken A, Kiwi-Minsker L (2011) Gas–liquid and liquid–liquid mass transfer in microstructured reactors. *Chem Eng Sci* 66(17):3876–3897
11. Hessel V, Angeli P, Gavriilidis A, Löwe H (2005) Gas–liquid and gas–liquid–solid microstructured reactors: contacting principles and applications. *Ind Eng Chem Res* 44(25):9750–9769
12. Chen G, Yue J, Yuan Q (2008) Gas-liquid microreaction technology: recent developments and future challenges. *Chin J Chem Eng* 16(5):663–669
13. Sobieszuk P, Aubin J, Pohorecki R (2012) Hydrodynamics and mass transfer in gas-liquid flows in microreactors. *Chem Eng Technol* 35(8):1346–1358
14. Lokhat D, Domah AK, Padayachee K, Baboolal A, Ramjugemath D (2016) Gas–liquid mass transfer in a falling film microreactor: effect of reactor orientation on liquid-side mass transfer coefficient. *Chem Eng Sci* 155:38–44
15. Noël T, Hessel V (2013) Membrane microreactors: gas-liquid reactions made easy. *ChemSusChem*. 6(3):405–407
16. Kurt SK, Warnebold F, Nigam KD, Kockmann N (2017) Gas-liquid reaction and mass transfer in microstructured coiled flow inverter. *Chem Eng Sci* 169:164–178
17. Abiev R, Svetlov S, Haase S (2017) Hydrodynamics and mass transfer of gas-liquid and liquid-liquid Taylor flow in microchannels. *Chem Eng Technol* 40(11):1985–1998
18. Kreutzer MT, Kapteijn F, Moulijn JA, Heiszwolf JJ (2005) Multiphase monolith reactors: chemical reaction engineering of segmented flow in microchannels. *Chem Eng Sci* 60(22):5895–5916
19. Hessel V, Renken A, Schouten JC, Yoshida J-I (eds) (2009) *Micro process engineering: a comprehensive handbook*. Wiley-VCH
20. Ehrfeld W, Hessel V, Löwe H (2000) *Microreactors: new technology for modern chemistry*. Weinheim, Wiley-VCH
21. Shao N, Gavriilidis A, Angeli P (2009) Flow regimes for adiabatic gas–liquid flow in microchannels. *Chem Eng Sci* 64(11):2749–2761
22. Triplett KA, Ghiaasiaan SM, Abdel-Khalik SI, Sadowski DL (1999) Gas–liquid two-phase flow in microchannels part I: two-phase flow patterns. *Int J Multiph Flow* 25(3):377–394
23. Nagy KD, Shen B, Jamison TF, Jensen KF (2012) Mixing and dispersion in small-scale flow systems. *Org Process Res Dev* 16(5):976–981
24. Plouffe P, Roberge DM, Macchi A (2016) Liquid–liquid flow regimes and mass transfer in various micro-reactors. *Chem Eng J* 300:9–19
25. Gordiychuk A, Svanera M, Benini S, Poesio P (2016) Size distribution and Sauter mean diameter of micro bubbles for a Venturi type bubble generator. *Exp Thermal Fluid Sci* 70:51–60
26. Rothstock S, Hessel V, Löb P, Werner B (2008) Characterization of a Redispersion microreactor by studying its dispersion performance. *Chem Eng Technol* 31(8):1124–1129
27. Tollkötter A (2016) *Mikrostrukturierte Baukastensysteme für Mehrphasenströmungen*. Dissertation. Schriftenreihe Apparatedesign. vol. 3: Verlag Dr. Hut
28. Reichmann F, Varel F, Kockmann N (2017) Energy optimization of gas–liquid dispersion in micronozzles assisted by Design of Experiment. *Processes*. 5(4):57
29. Reichmann F, Koch M-J, Kockmann N. Investigation of Bubble Breakup in Laminar, Transient, and Turbulent Regime Behind Micronozzles. In: Proc. ASME 15th Int. Conf. Nano, Micro, and Minichannels - 2017: August 27–30, 2017, Cambridge, Massachusetts, USA. V001T03A001
30. Reichmann F, Koch M, Körner S, Kockmann N. Internal Jet Formation During Bubble Generation in Microchannels. In: Proc. ASME 15th Int. Conf. Nano, Micro, and Minichannels - 2017: August 27–30, 2017, Cambridge, Massachusetts, USA. V001T08A002
31. Yue J, Chen G, Yuan Q, Luo L, Gonthier Y (2007) Hydrodynamics and mass transfer characteristics in gas–liquid flow through a rectangular microchannel. *Chem Eng Sci* 62(7):2096–2108
32. Yang L, Dietrich N, Loubière K, Gourdon C, Hébrard G (2016) Visualization and characterization of gas–liquid mass transfer around a Taylor bubble right after the formation stage in microreactors. *Chem Eng Sci* 143:364–368
33. Zhu C, Lu Y, Fu T, Ma Y, Li HZ (2017) Experimental investigation on gas-liquid mass transfer with fast chemical reaction in microchannel. *Int J Heat Mass Tran* 114:83–89
34. Yang L, Tan J, Wang K, Luo G (2014) Mass transfer characteristics of bubbly flow in microchannels. *Chem Eng Sci* 109:306–314
35. Chu C, Zhang F, Zhu C, Fu T, Ma Y (2019) Mass transfer characteristics of CO₂ absorption into 1-butyl-3-methylimidazolium tetrafluoroborate aqueous solution in microchannel. *Int J Heat Mass Trans* 128:1064–1071
36. Nieves-Remacha MJ, Jensen KF (2015) Mass transfer characteristics of ozonolysis in microreactors and advanced-flow reactors. *J Flow Chem* 5(3):160–165
37. Dietrich N, Loubière K, Jimenez M, Hébrard G, Gourdon C (2013) A new direct technique for visualizing and measuring gas–liquid mass transfer around bubbles moving in a straight millimetric square channel. *Chem Eng Sci* 100:172–182
38. Awad MM. Two-phase flow. In: Kazi MSN, editor. *An Overview of Heat Transfer Phenomena*. InTech, 2012

39. Garstecki P, Stone HA, Whitesides GM (2005) Mechanism for flow-rate controlled breakup in confined geometries: a route to monodisperse emulsions. *Phys Rev Lett* 94(16):164501
40. Jensen KF, Reizman BJ, Newman SG (2014) Tools for chemical synthesis in microsystems. *Lab Chip* 14(17):3206–3212
41. Sato K, Tokeshi M, Sawada T, Kitamori T (2000) Molecular transport between two phases in a microchannel. *Anal Sci* 16(5):455–456
42. Kockmann N (2008) Transport phenomena in micro process engineering. Heat and mass transfer. Springer
43. Matsuyama K, Mine K, Kubo H, Aoki N, Mae K (2010) Optimization methodology of operation of orifice-shaped micromixer based on micro-jet concept. *Chem Eng Sci* 65(22):5912–5920
44. Fu T, Ma Y, Funfschilling D, Zhu C, Li HZ (2010) Squeezing-to-dripping transition for bubble formation in a microfluidic T-junction. *Chem Eng Sci* 65(12):3739–3748
45. Andersson R, Andersson B (2006) On the breakup of fluid particles in turbulent flows. *AICHE J* 52(6):2020–2030
46. Field BS, Hmjak PS. Two-Phase Pressure Drop and Flow Regime of Refrigerants and Refrigerant-Oil Mixtures in Small Channels., 2009
47. VDI-GVC, ed. VDI Heat Atlas (2nd edition). VDI-Buch. Berlin: Springer, 2010
48. Yang L, Dietrich N, Hébrard G, Loubière K, Gourdon C (2017) Optical methods to investigate the enhancement factor of an oxygen-sensitive colorimetric reaction using microreactors. *AICHE J* 63(6):2272–2284
49. Reichmann F, Tollkötter A, Körner S, Kockmann N (2017) Gas-liquid dispersion in micronozzles and microreactor design for high interfacial area. *Chem Eng Sci* 169:151–163
50. Ghaini A, Mescher A, Agar DW (2011) Hydrodynamic studies of liquid–liquid slug flows in circular microchannels. *Chem Eng Sci* 66(6):1168–1178
51. Krieger W, Lamsfuß J, Zhang W, Kockmann N (2017) Local mass transfer phenomena and chemical selectivity of gas-liquid reactions in capillaries. *Chem Eng Technol* 40(11):2134–2143
52. Abadie T, Aubin J, Legendre D, Xuereb C (2012) Hydrodynamics of gas–liquid Taylor flow in rectangular microchannels. *Microfluid Nanofluid* 12(1–4):355–369
53. Thulasidas TC, Abraham MA, Cerro RL (1997) Flow patterns in liquid slugs during bubble-train flow inside capillaries. *Chem Eng Sci* 52(17):2947–2962
54. Gupta R, Fletcher DF, Haynes BS (2010) Taylor flow in microchannels: a review of experimental and computational work. *Int J Multiphase Flow* 2(1):1–31
55. Berčić G, Pintar A (1997) The role of gas bubbles and liquid slug lengths on mass transport in the Taylor flow through capillaries. *Chem Eng Sci* 52(21–22):3709–3719
56. Mikaelian D, Haut B, Scheid B (2015) Bubbly flow and gas–liquid mass transfer in square and circular microchannels for stress-free and rigid interfaces: CFD analysis. *Microfluid Nanofluid* 19(3):523–545
57. Reichmann F, Continuous reaction Calorimetry for intensified reaction systems. Dissertation. Schriftenreihe Apparatedesign. 13: Verlag Dr. Hut, 2020

Publisher's note Springer Nature remains neutral with regard to jurisdictional claims in published maps and institutional affiliations.